Journal of Materials Chemistry C

ROYAL SOCIETY OF CHEMISTRY

PAPER

View Article Online
View Journal | View Issue

Cite this: J. Mater. Chem. C, 2024, 12, 1851

Revealing the essential effect mechanism of carbon nanotubes on the thermal conductivity of graphene film†

Yu-Ze Xing,‡[ab] Meng Li,‡[ab] Hui Jia,[a] Li-Jing Xie,[a] Dong Liu,[ab] Zheng Wang,[ab] Ze-Chao Tao,[a] Ye-Long Tong,[d] Qing-Qiang Kong*[a] and Cheng-Meng Chen *[ac]

Received 21st October 2023,
Accepted 10th December 2023

DOI: 10.1039/d3tc03840h

rsc.li/materials-c

The inclusion of carbon nanotubes (CNTs) should increase the thermal conductivity (TC) of graphene films. However, this notion still remains controversial and the effect mechanism of CNTs on the TC of graphene films is uncertain. Here, graphene films with different CNT loadings are fabricated to reveal the effect mechanism of CNTs. After graphitization of the as-obtained films, lattice distortion occurs and the defect density increases from 1.57 × 10^{10} cm^{-2} to 3.73 × 10^{10} cm^{-2} due to the addition of CNTs. Moreover, the introduction of CNTs induces the generation of C=C bonds between the CNTs and graphene. Molecular dynamic simulation proves that the existence of C=C bonds reduces the in-plane thermal conductivity (IP-TC). The measurement results from different equipment further demonstrate the decreasing trend of the IP-TC with the increment of the CNT content. Conversely, the out-of-plane thermal conductivity (OP-TC) increases from 0.5 W $(m\ K)^{-1}$ to 3.5 W $(m\ K)^{-1}$ and the elastic modulus decreases from 2.86 GPa to 71.69 MPa. Thus, the graphene/CNT hybrid film is more suitable as a thermal interface material at high temperatures (>200 °C), rather than heat spreader materials. The work provides a more in-depth understanding and a new application route for graphene/CNT films.

1. Introduction

Graphene film has been widely applied in the thermal management of electronic equipment owing to its outstanding TC, lightweight, flexibility, and anti-corrosion.[1–7] In particular, integrated devices with high heat flux urgently demand graphene films with higher TC.[8] The enhancement of TC is required to construct more thermal conduction pathways in graphene films. Currently, an intuitive notion has emerged: the thermal conduction path of graphene films is further increased by adding one-dimensional materials, for instance CNTs, carbon fibers and cellulose.[9–11] Among them, CNTs are often used as fillers to increase thermal pathways due to their intrinsically high TC,[12–14] improving the IP-TC of graphene films.[15–17]

In past research, two diverse trends have been reported regarding the effect of CNTs on the IP-TC of graphene films. One point of view is that the IP-TC of graphene/CNT films increases at first and then decreases with the increment of the CNT content, thereby exhibiting an optimal dosage of CNTs. For example, the maximum IP-TC of a graphene/CNT film reaches 1154 W $(m\ K)^{-1}$ after graphitization when the CNT content is 20 wt%.[16] Similarly, the optimal IP-TC of the graphene/CNT film is 1388.7 W $(m\ K)^{-1}$ after treating at 1000 °C with CNTs of 15 wt%.[10] The above studies suggest that the introduction of the CNTs, with content less than the threshold, benefits the construction of the thermal conduction path, which enhances the phonon transport channel and improves the IP-TC of the graphene film. When the CNT content exceeds the threshold, the phonon scattering induced by CNT agglomeration results in larger interfacial thermal resistance and lower IP-TC of the graphene film.[10,16]

However, another point of view is that the addition of CNTs reduces the IP-TC of the hybrid film. For instance, the IP-TC of the hybrid film monotonically decreases to 35.2 W $(m\ K)^{-1}$ when the CNT content increases to 70 wt% after 1100 °C treatment.[18] Likewise, when the CNT content gradually increases from 0 wt% to 35 wt%, the IP-TC of the hybrid film decreases from 836.8 W $(m\ K)^{-1}$ to 414.61 W $(m\ K)^{-1}$.[19] The above research considers that the existence of defects and

[a] CAS Key Laboratory of Carbon Materials, Institute of Coal Chemistry, Chinese Academy of Sciences, Taiyuan, 030001, China. E-mail: kongqq@sxicc.ac.cn, ccm@sxicc.ac.cn
[b] University of Chinese Academy of Sciences, Beijing 100049, China
[c] Center of Materials Science and Optoelectronics Engineering, University of Chinese Academy of Sciences, Beijing 100049, China
[d] Beijing Institute of Spacecraft System Engineering, Beijing, 100094, China

† Electronic supplementary information (ESI) available. See DOI: https://doi.org/10.1039/d3tc03840h

‡ Yu-Ze Xing and Meng Li contributed equally to this work.

boundaries between CNTs and graphene sheets causes phonon scattering, thereby reducing the IP-TC of the graphene film. Despite the abundant studies, the two trends are different so that the effect mechanism of CNTs on the IP-TC of graphene film did not reach a consensus. Therefore, a more in-depth systematic study of the effect mechanism of CNTs on the IP-TC of graphene film is still lacking.

Herein, the effect mechanism of the CNTs on the IP-TC of graphene film was systematically explored by investigating the air gap, crystallinity, defects, and covalent bonds using the experimental analysis method and molecular dynamics simulation. The thermal diffusivity of the graphene/CNT film with different CNT loading was evaluated by laser flash after eliminating humans and equipment differences. The IP-TC of the graphene/CNT films was calculated at the same density, showing a monotonously decreasing trend with the increase of the CNTs. A new application route was proposed by testing the out-of-plane thermal diffusivity and elastic modulus. This paper provides a comprehensive understanding for the construction of thermal management materials by one-dimensional carbon nanomaterials and two-dimensional graphene.

2. Experiments

2.1 Preparation of the graphene/CNT film

Firstly, a homogeneous CNT solution of 2 mg mL^{-1} was obtained by dissolving 100 mg of CNT powder in 50 mL of deionized water using an ultrasonic process (700 W, 30 min). GO slurry (2 mg mL^{-1})[20–22] and CNT solution (2 mg mL^{-1}) (ESI†) with different volumes were mixed to obtain homogeneous mixed solutions by ultrasonication (700 W, 30 min). The total solid mass of the mixture was 200 mg. The mass fraction of CNTs in the GO/CNT mixture was 1 wt%, 3 wt%, 5 wt%, and 15 wt%, respectively (Table S1, ESI†). In Fig. 1a, the GO film and GO/CNT films were obtained by vacuum filtration on nylon-66 filtrate paper (pore size of 0.45 μm, 23.5 mm in radius, Whatman). Finally, the above films were dried at 45 °C to obtain GO film (GOF) and GO/CNT films (GO/CF-1, GO/CF-3, GO/CF-5, and GO/CF-15).

The obtained films were treated at 700 °C (Ar atmosphere) in a tube furnace to get reduced GO film and reduced GO/CNT films. Then, they were further graphitized at 2800 °C (4 h, Ar atmosphere) and compressed under 30 MPa to get the graphene film and the graphene/CNT film. According to the mass fraction of CNTs in the mixture, the reduced GO film and the reduced GO/CNT film were labeled as rGOF, rGO/CF-1, rGO/CF-3, rGO/CF-5, and rGO/CF-15, respectively. Similarly, the graphene/CNT films were named G/CNF-1, G/CNF-3, G/CNF-5, and G/CNF-15, respectively, and the graphene film was labeled as GF.

2.2 Characterization

The crystallinity and micromorphology of all films was analyzed by High-resolution transmission electron microscopy (HRTEM, Japan, JEOL JEM-2100F) and field-emitting scanning electron microscopy (SEM, Japan, JSM-7900F). Atomic force microscopy (AFM, Germany, Burke Innova) was used to assess the size of the GO sheets. Crystal structure information was obtained using the silicon internal standard method by X-ray diffraction (XRD, Japan, XtaLAB mini™ II) with a scan speed of 5° min^{-1}. The silicon internal standard method was utilized to accurately characterize the structural information of graphene films by grinding the mixture of graphene film and high crystalline silicon powder. The defect information of the films was studied by Raman spectroscopy (Raman, Japan, LabRAM HR Evolution). The sp^2 carbon and sp^3 carbon of the film were investigated by X-ray photoelectron spectroscopy (XPS, USA, Thermo Kalpha, Al Kα). Thermogravimetric analysis (TGA) measurements (TG, Japan, J300) were performed from 30 to 1000 °C at a heating rate of 10 °C min^{-1} in an Air atmosphere. The thermal conductivity of the film was calculated by testing the thermal diffusivity (α), specific heat (C_p, 850 J (kg K)$^{-1}$), and sample density (ρ) (details in ESI†). The elastic modulus was measured by a NanoIndentor (Hysitron TS 77 Select, Germany). Molecular dynamics simulation was used to further study the effect of covalent bonds on the IP-TC of the graphene film. The theoretical model consists of two systems, monolayer graphene with a single CNT representing G/CNF and monolayer graphene representing GF. The supercell size of the graphene sheet model is 10 nm × 10 nm in the *XY* plane, and the length and diameter of the CNTs are 8.2 nm and 1.2 nm. Tersoff potential was utilized to represent the covalent bonds between C atoms.[23] According to the Green–Kubo formula, the TC was calculated by the equilibrium molecular dynamics method using the heat flux auto-correlation function (eqn (1)):

$$K = \frac{1}{K_B T^2}\int_0^\infty \langle J_{E_x}(0) J_{E_x}(t)\rangle \mathrm{d}t \quad (1)$$

where K_B, T, and J_{E_x} represent the Boltzmann constant, the systematic temperature, and the x direction component of the heat flux component J_E. The TC value was calculated for each component of the heat flux in the x and y direction, and the final calculated value takes the average of these two values. The TC was simulated under the NVT ensemble. The correlation length of the auto-correlation function was 20 ps, and a total of 1 million steps was calculated.

3. Results and discussion

3.1 Morphology of all films

The size of the GO sheets was investigated by AFM. The thickness is 1.069 nm and the lateral size is about 3–5 μm (Fig. S3, ESI†), showing that GO sheets are close to monolayer GO.[22] The micromorphology of the films was characterized using SEM (Fig. 1b–g). The cross-sectional image of G/CNF-5 exhibits a layer-by-layer structure as in past reports,[10] and the thickness of the G/CNF-5 is 46 μm (Fig. 1b). High magnification SEM images of GOF, GO/CF-1, GO/CF-3, GO/CF-5, and GO/CF-15 show CNTs intercalated between graphene sheets (Fig. 1c–g), leading to the formation of air gaps. In addition, the volume of the air gap increases with the increase in carbon nanotube content. The air gap reduces the densification of the graphene film after graphitization (Fig. S5a, ESI†). Moreover, the connection points increase (Fig. S1a–e, ESI†), and more agglomeration

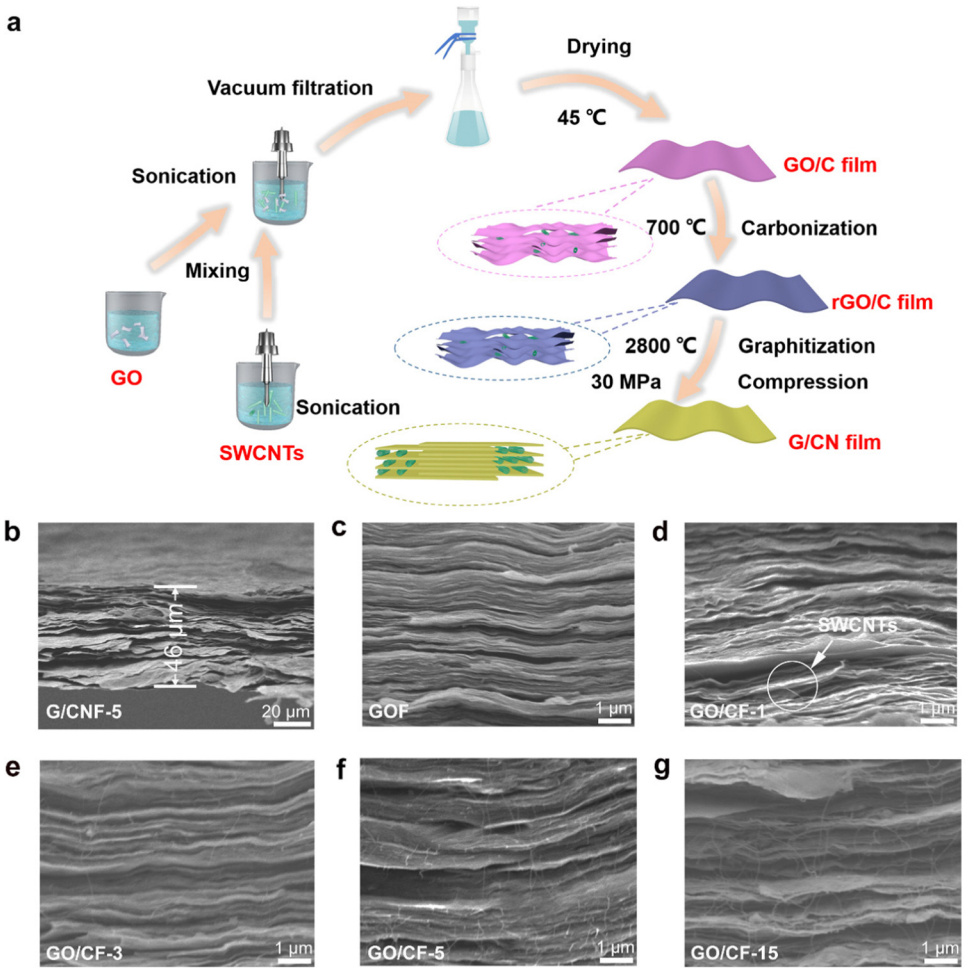

Fig. 1 (a) Fabrication schematic of the GO/CF, rGO/CF, and G/CNF. (b) Cross-sectional SEM image of G/CNF-5. Higher magnification SEM pictures of (c) GOF, (d) GO/CF-1, (e) GO/CF-3, (f) GO/CF-5, and (g) GO/CF-15.

also occurs due to the introduction of more CNTs (Fig. S2a–e, ESI†), which forms more boundaries. It is not conducive to the phonon transport of the graphene film.

3.2 Structural characterization

The graphitization structure evolution and defect information of the films were investigated by XRD and Raman spectroscopy. The standard diffraction angle ($2\theta_c$) of the films with different CNT amounts is calculated from the diffraction angle ($2\theta_{Si}$) of the standard silicon using the silicon internal standard method (Fig. 2a) (Formula S1, ESI†).[24] The $2\theta_c$ of the (002) plane decreases from 26.49° to 26.42° with the rising of the CNT content (Table 1). According to the Braggs equation, the corresponding interlayer *d*-spacing reduces to 0.337 nm from 0.336 nm (Table 1).[25] The grain size (L_c) was calculated from XRD by using the Scherrer equation (Formula S2, ESI†). As shown in Table 1, the crystallite size (L_c) of GF, G/CNF-1, G/CNF-3, G/CNF-5, and G/CNF-15 is 25.35 nm, 25.28 nm, 22.04 nm, 21.32 nm and 24.51 nm, respectively, which indicates that the films have a large grain size in the *C*-axis direction. Meanwhile, the graphitization degree of the films is also explored by Mering–Maire (Formula S3, ESI†), which gradually reduces from 90.7% (GF) to 80.5% (G/CNF-15) (Table 1).[26,27] The results demonstrate that the insertion of CNTs disturbs the orderly stacking of graphene sheets, which is adverse to the improvement of TC of hybrid films.[28] Furthermore, the peak area ratio of the D-band to the G-band (I_D/I_G) was calculated from the Raman results (Fig. 2b), which represents structural defects. The I_D/I_G increases from 0.07 to 0.166 as the CNTs increase from 0 wt% to 15 wt% (Fig. 2b), indicating an increase of defect concentration.[29,30] The defect distance (L_D) (Formula S4, ESI†) and defect density (n_D) (Formula S5, ESI†) are further calculated (Fig. 2c). The defect density increases from 1.57×10^{10} cm^{-2} to 3.73×10^{10} cm^{-2}, while the defect distance decreases from 45.38 nm to 29.47 nm.[31,32] This is attributed to the junction between graphene sheets and CNTs that provides more sites for the formation of defects with the increment of the CNT content. The increment of the defects leads to the strong scattering of all phonon modes.[33] Moreover, the defects inevitably decrease the crystallinity of the graphene film. The crystallite size (L_a) is calculated by Cançado (Formula S6, ESI†).[22] As shown in Table 1, the crystallite size (L_a) decreases from 274.6 nm to 115.8 nm as the CNTs increase from 0 wt% to 15 wt%, indicating that the addition of CNTs hinders the

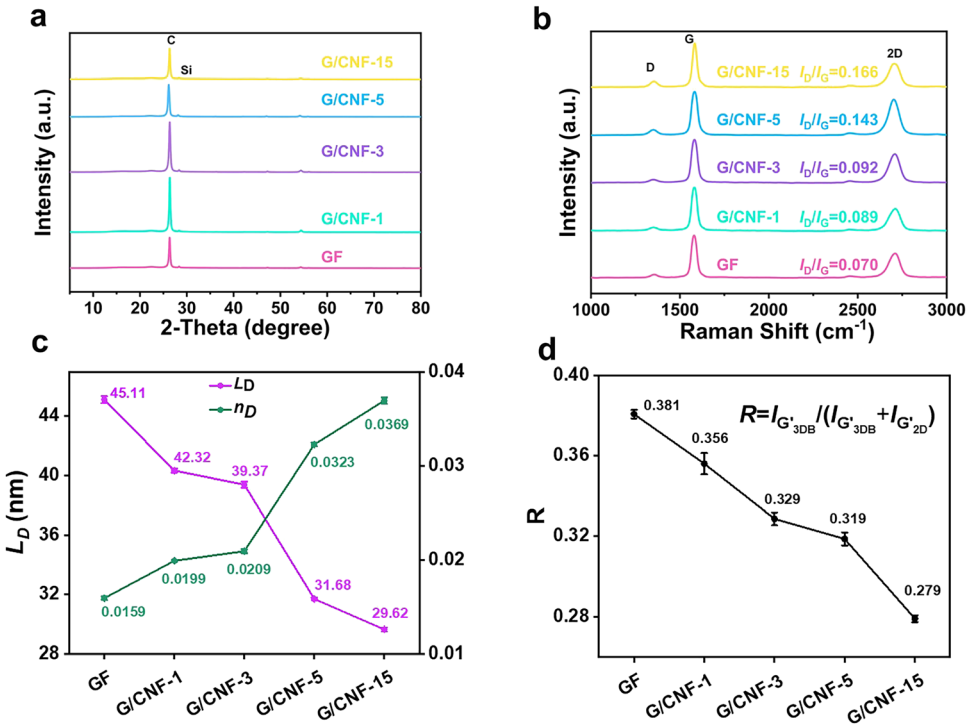

Fig. 2 (a) XRD patterns, (b) Raman spectrum of GF, G/CNF-1, G/CNF-3, G/CNF-5, and G/CNF-15. (c) The defect distance (L_D) and defect density (n_D) of GF, G/CNF-1, G/CNF-3, G/CNF-5, and G/CNF-15. (d) The R value of GF, G/CNF-1, G/CNF-3, G/CNF-5, and G/CNF-15.

Table 1 Structural parameters of GF, G/CNF-1, G/CNF-3, G/CNF-5, and G/CNF-15

Samples	GF	G/CNF-1	G/CNF-3	G/CNF-5	G/CNF-15
$d_{(002)}$/nm	0.3362	0.3365	0.3368	0.3370	0.3370
G (%)	90.7	87.2	83.7	81.4	80.5
I_D/I_G	0.070	0.089	0.092	0.143	0.166
L_c (nm)	25.35	25.28	22.04	21.32	24.51
L_a (nm)	274.6	216.0	208.9	134.4	115.8

growth of graphene crystallites. The reduction of L_a greatly aggravates low-frequency phonon scattering. Furthermore, a 2D peak presents at 2700 cm^{-1} due to structural transformation from the amorphous structure to crystalline carbon in the graphitization process (Fig. S6a–e, ESI†). The symmetrical 2D peak observed in the Raman spectroscopy of all films shows the existence of a turbostratic stacking structure. To confirm the proportion of turbostratic and Bernal stacking, the 2D peak is fitted into three Lorentzian peaks: G'_{2D} representing turbostratic stacking, and G'_{3DA} and G'_{3DB} representing Bernal stacking.[34–36] The fraction R is calculated according to the inset formula in Fig. 2d, which represents the proportion of Bernal stacking in the films. The value of R decreases from 0.38 to 0.28 as the CNTs increase from 0 wt% to 15 wt%, revealing that the intercalation of CNTs induces the transition from ordered arrangement to disorder arrangement of the graphene sheets. This can result in weak interlayer binding energy, thereby decreasing the phonon interfacial scattering.[28]

To determine the change of covalent bond type of the film, the ratio of sp^2 to sp^3 carbon (c_{sp^2}/c_{sp^3}) was studied by XPS (Fig. 3b–f). The C 1s of XPS is fitted to three components: C–C sp^2 carbon (284.7 eV), C–C sp^3 carbon (285.4 eV) and π–π* shake-up peak (290.3 eV) (the specific peak fitting process is in the ESI†).[37,38] With the increment of the CNT content from 0 wt% to 15 wt%, the c_{sp^2}/c_{sp^3} gradually increases from 1.30 (GF) to 2.83 (G/CNF-15) (Fig. 3b–f). Because CNTs and graphene film have different c_{sp^2}/c_{sp^3} values after graphitization (Fig. 3a and b), the sp^2 and sp^3 carbon contents of the graphitized graphene film and CNTs were analyzed (Table S3, ESI†). To eliminate the increase of c_{sp^2}/c_{sp^3} caused by the blending of the CNTs, the theoretical values of the ratio of hybrid films were calculated by the following eqn (2):

$$c_{sp^2}/c_{sp^3}(t) = \frac{(c_{sp^2}(G) \times (1-x) + c_{sp^2}(C) \times x)}{(c_{sp^3}(G) \times (1-x) + c_{sp^3}(C) \times x)} \quad (2)$$

where c_{sp^2} (G), c_{sp^2} (C), c_{sp^3} (G), c_{sp^3} (C), and x represent the amount of sp^2 carbon in the graphene film, the amount of sp^2 carbon in the CNT powder after graphitization, the amount of sp^3 carbon in the graphene film, the amount of sp^3 carbon in the CNT powder after graphitization, and the mass fraction of CNTs in the hybrid film. The experimental ratio values ($c_{sp^2}/c_{sp^3}(e)$) of the hybrid film are obviously larger than the theoretical ratio values ($c_{sp^2}/c_{sp^3}(t)$) (Table 2), which provides evidence for the generation of C=C covalent bonds between the CNTs and graphene sheets. The C=C bond between the graphene sheets and CNTs will aggravate the phonon scattering in the graphene sheets, while it will provide transport channels for phonons between the graphene sheets.[39,40]

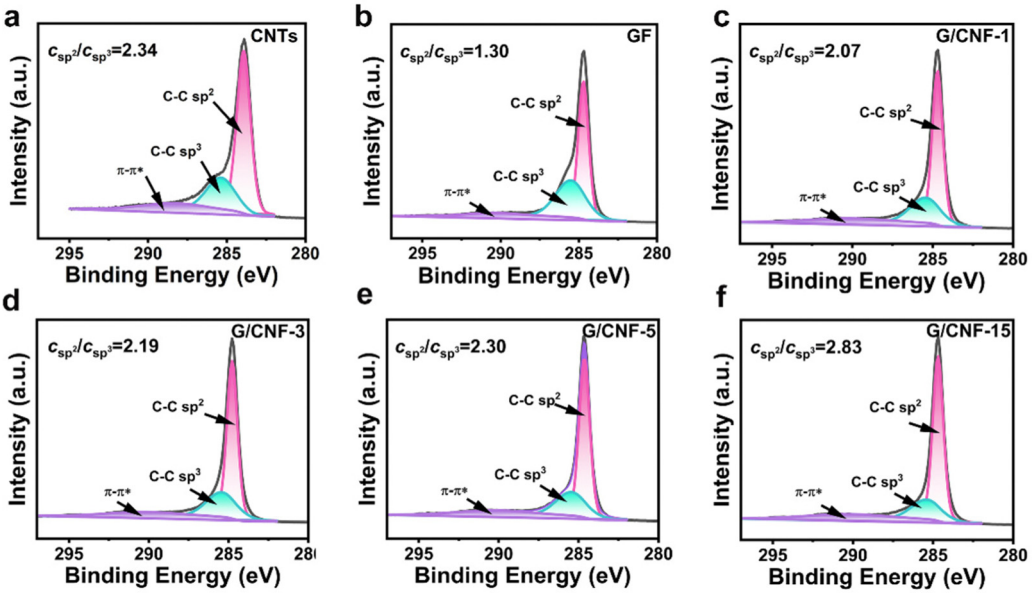

Fig. 3 C 1s XPS spectrum of (a) CNTs, (b) GF, (c) G/CNF-1, (d) G/CNF-3, (e) G/CNF-5, and (f) G/CNF-15.

Table 2 Bond parameters of CNTs, GF, G/CNF-1, G/CNF-3, G/CNF-5, and G/CNF-15

Samples	CNTs	GF	G/CNF-1	G/CNF-3	G/CNF-5	G/CNF-15
$c_{sp^2}/c_{sp^3}(e)$	2.34	1.30	2.07	2.19	2.30	2.83
$c_{sp^2}/c_{sp^3}(t)$	2.34	1.30	1.30	1.30	1.31	1.34

Notes: *e*: experimental ratio values; *t*: theoretical ratio values.

3.3 The evolution of graphitization structure and molecular dynamics simulations

To further verify the effect of CNTs on the lattice structure of the graphene films, HRTEM was used to reveal the crystallinity and structural integrity of GF and G/CNF-15 (Fig. 4a–d). In Fig. 4a, the long-range ordered lattice is observed in GF, indicating the high crystallinity of the graphene sheets after graphitization. Also, the defect-free ordered honeycomb lattice structure indicates that the defects were almost completely repaired after graphitization (Fig. 4b), which corresponds to the results of XRD and Raman. Compared with GF, lattice distortion appears adjacent to the CNTs and graphene sheets in G/CNF-15 (the blue line in Fig. 4c), which can be used to illustrate the reduction of crystallinity. Also, the fracture of CNTs and the disordered alignment of partial carbon atoms occurs at the junction (Fig. 4d), which further proves the generation of covalent bonds between the graphene and CNTs (Fig. 4c). Based on the XPS, HRTEM results and previous research,[40–43] we constructed a composite model of monolayer graphene with a single CNT (Fig. 4e and f) and a model of monolayer graphene (Fig. S4, ESI†), which represents G/CNF and GF structure, respectively. The TC in the *x* and *y* directions is calculated by simulating the heat flux of the system, and the final TC is obtained by the average value of two values. As shown in Fig. 4g, the IP-TC of GF is 1541.68 W (m K)$^{-1}$, which is higher than G/CNF (1246.13 W (m K)$^{-1}$). This is attributed to the fact that the covalent bonds induce the occurrence of severe phonon energy localization and the poor coordination of phonon vibration, thereby reducing the IP-TC of the graphene film.

3.4 Thermal performance and mechanical performance

To concretely investigate the effect of CNTs on the TC of the graphene film, the thermal diffusivity of the graphene/CNT films was tested by the laser flash method. The addition of CNTs enhances the out-of-plane thermal diffusivity of graphene films due to the connection between the CNTs and graphene. The out-of-plane thermal diffusivity reaches 2.9 mm^2 s^{-1} at a CNT content of 15 wt%, which is 966% of pure graphene films (0.3 mm^2 s^{-1}) (Fig. 5a). The introduction of CNTs provides more channels for phonon transfer in the *Z*-axial direction. However, the density of the films is also critical for TC. The introduction of different amounts of CNTs causes more air gaps. The presence of air gaps affects the densification of the graphene film, leading to an increased thickness of the graphene film from about 46 μm to 70 μm (Fig. S5b, ESI†). The corresponding density decreases from 1.95 g cm^{-3} (GF, G/CNF-1, G/CNF-3, and G/CNF-5) to 1.43 g cm^{-3} (G/CNF-15) (Fig. S5a, ESI†). When the CNT content reaches 15 wt% in the hybrid film, the OP-TC of G/CNF-15 is lower than that of G/CNF-5. Furthermore, the elastic modulus decreases from 2.86 GPa to 71.69 MPa as the CNT content increases from 0 wt% from 15 wt% (Table S2, ESI†). This is attributed to the fact that CNTs with a one-dimension tubular structure act as a support between the graphene sheets, reducing the elastic modulus of the hybrid films (Fig. 5b). Unfortunately, the IP-TC of the graphene/CNTs films shows a decreasing trend. To eliminate differences caused by equipment and operator, a series of in-plane thermal diffusivity values were tested through different

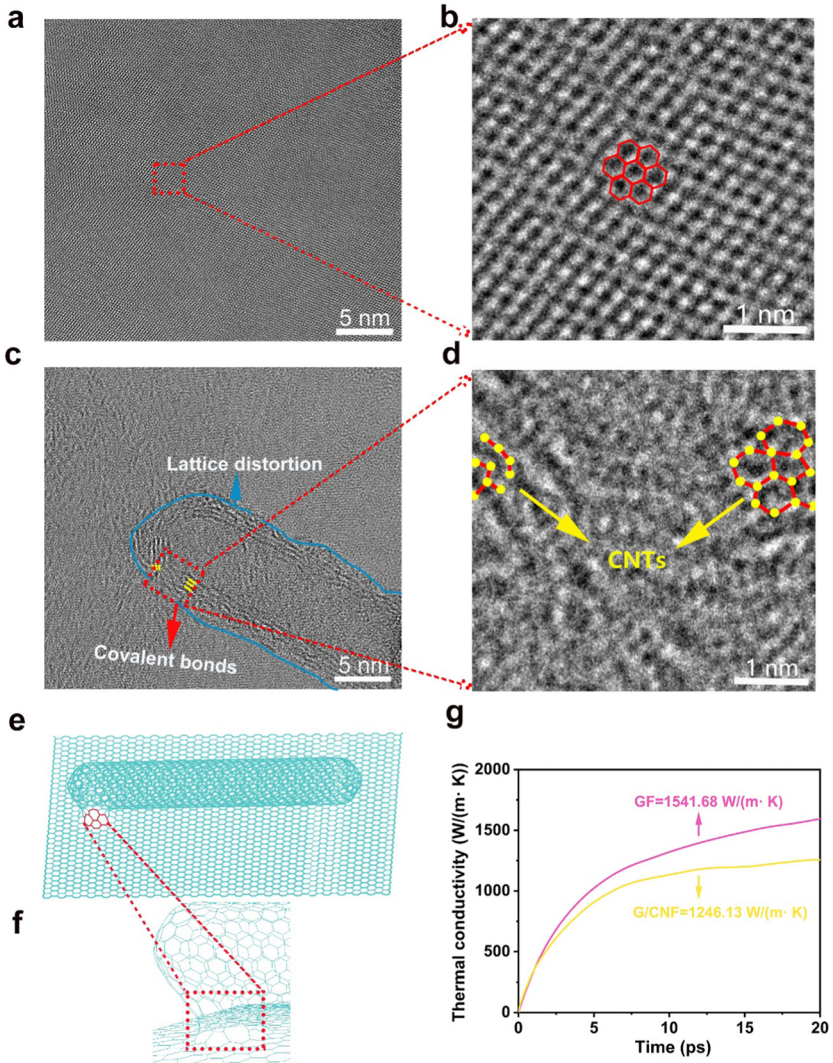

Fig. 4 HRTEM pictures of (a) and (b) GF and (c) and (d) G/CNF-15. The simulation domain has 10 nm × 10 nm × 10 nm in three-dimensional space. (e) and (f) Models and connection location view of the G/CNF structure (monolayer graphene with a single CNT). (g) The IP-TC of GF and G/CNF according to molecular dynamics simulation.

equipment in different laboratories. The result from the LFA 467 test shows that the in-plane thermal diffusivity decreases from 540.1 $mm^2\ s^{-1}$ to 380 $mm^2\ s^{-1}$ as the CNT content increases from 0 wt% to 5 wt% (Fig. 5c). Similarly, the test result of LFA 447 also shows the same trend with the in-plane thermal diffusivity decreasing from 487.4 $mm^2\ s^{-1}$ to 378.4 $mm^2\ s^{-1}$ (Fig. 5d). For previous studies, the IP-TC of graphene/CNT films can reach a maximum when the amount of CNTs is 15 wt% or 20 wt%, so the hybrid film with loading 15 wt% CNTs (G/CNF-15) was prepared as a control in this work. The IP-TC of G/CNF-15 is 194.2 $mm^2\ s^{-1}$ (LFA 447) and 288.8 $mm^2\ s^{-1}$ (LFA 467), respectively, which is much lower than that of G/CNF-5 (Fig. 5c and d). Based on the above in-plane thermal diffusivity and density, the IP-TC of the hybrid films is further calculated (Fig. 5c and d). With the increment of the CNTs, the IP-TC of the film decreases from 895.2 $W\ (m\ K)^{-1}$ (LFA 467) to 478.7 $W\ (m\ K)^{-1}$ (LFA 467) at room temperature (Fig. 5c) For the above research, the addition of CNTs reduces the TC of the graphene film, which can be determined by the following reasons (Fig. 5e):

Firstly, the CNTs reduce the graphitization degree of the graphene film from 90.7% to 80.5% and increase the defects density from 1.57 × 10^{10} cm^{-2} to 3.73 × 10^{10} cm^{-2}. The existence of defects leads to strong low frequency phonon scattering, which possesses a long mean free path and makes a dominant contribution to the TC. When the defects inside the hybrid films increase, the long-MFP phonons are further suppressed, resulting in a further decrease in TC. Secondly, the generation of covalent bonds between graphene and CNTs induces the occurrence of phonon energy localization at the junction between graphene and CNTs, and the mismatch of phonon vibration, destroying the phonon transport. Thirdly, the intercalation of excess CNTs into graphene sheets easily results in the formation of air gaps, which reduces the density of the graphene film. Meanwhile, the TC of air (0.026 $W\ (m\ K)^{-1}$) is far lower than that of graphene,[44] resulting

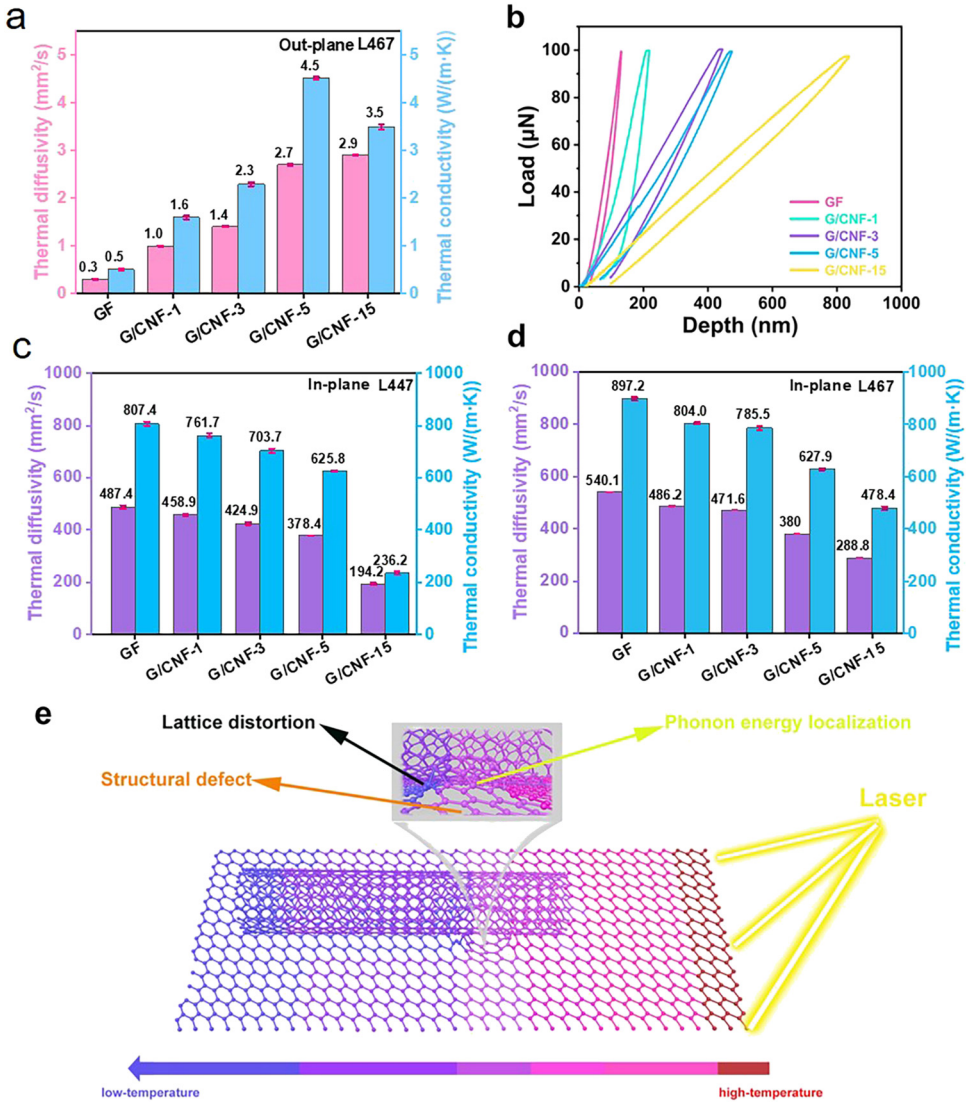

Fig. 5 (a) Out-of-plane thermal diffusivity (pink) and OP-TC (light blue) of GF, G/CNF-1, G/CNF-3, G/CNF-5, and G/CNF-15 using LFA 467. (b) Elastic modulus of GF, G/CNF-1, G/CNF-3, G/CNF-5, and G/CNF-15. (c) In-plane thermal diffusivity (purple) and IP-TC (blue) of GF, G/CNF-1, G/CNF-3, G/CNF-5, and G/CNF-15 using LFA 467. (d) In-plane thermal diffusivity (purple) and IP-TC (blue) of GF, G/CNF-1, G/CNF-3, G/CNF-5, and G/CNF-15 using LFA 447. (e) Schematic of the effect mechanism of CNTs on graphene heat transfer.

in a decrease in the IP-TC of the graphene film. Although the introduction of CNTs reduces the in-plane heat transfer performance of the hybrid films, it enhances the out-of-plane heat transfer performance and decreases the elastic modulus of the hybrid films, providing an application chance for thermal interface materials at high temperature (Fig. S7, ESI†).

4. Conclusions

In summary, the effect mechanism of CNTs on the graphitized carbon nano-architecture and the TC of graphene films was revealed. With the addition of CNTs, the defect density increases from 1.57×10^{10} cm^{-2} to 3.73×10^{10} cm^{-2}, and the crystallite size decreases from 274.6 nm to 115.8 nm. Furthermore, the generation of covalent bonds between graphene and CNTs causes lattice distortion of the graphene sheets, thereby aggravating low-frequency phonon scattering. Also, molecular dynamics simulation proves that the formation of covalent bonds reduces the IP-TC of the graphene film. As the CNT content increases from 0 wt% to 15 wt%, the IP-TC of the films shows a decreasing trend. The OP-TC increases from 0.5 W (m K)$^{-1}$ to 4.5 W (m K)$^{-1}$ at the same density. The elastic modulus decreases from 2.86 GPa to 220.66 MPa. Therefore, graphene/CNT hybrid film is not suitable for thermal spreader materials but for thermal interface materials. This study provides an in-depth cognition of the effect mechanism of CNTs on thermal conductivity and a future practical application route of thermal interface materials.

Author contributions

Yu-Ze Xing: investigation, formal analysis, data curation, writing – original draft, writing – review & editing, validation,

methodology. Meng Li: investigation, formal analysis, data curation, writing – original draft, writing – review & editing, validation, methodology, software. Hui Jia: resources, writing – original draft, formal analysis, writing – review & editing, project administration. Li-Jing Xie: writing – original draft, writing e review & editing, project administration, funding acquisition. Dong Liu: investigation, formal analysis, data curation, software. Zheng Wang: investigation, formal analysis, methodology. Ze-Chao Tao: resources, formal analysis, project administration. Ye-Long Tong: formal analysis, project administration. Qing-Qiang Kong: resources, writing – original draft, formal analysis, writing – review & editing, project administration. Cheng-Meng Chen: conceptualization, resources, project administration, supervision, funding acquisition.

Conflicts of interest

There are no conflicts to declare.

Acknowledgements

This research was supported by the National Natural Science Foundation of China (52202055), Scientific and Technological Key Project of Shanxi Province (202101040201005), National Natural Science Foundation of China (22379157). Fundamental Research Program of Shanxi Province (20210302124101). Research and Development (R&D) of lightweight carbon nano-microwave absorption/thermal insulation composites, Key Research and Development (R&D) Projects of Shanxi Province (2022ZDYF027) and Research Project Supported by ICC CAS,SCJC-XCL-2023-12.

References

1 A. Akbari, B. V. Cunning, S. R. Joshi, C. Wang, D. C. Camacho-Mojica, S. Chatterjee, V. Modepalli, C. Cahoon, C. W. Bielawski, P. Bakharev, G.-H. Kim and R. S. Ruoff, *Matter*, 2020, **2**, 1198–1206.
2 S. Chen, Q. Wang, M. Zhang, R. Huang, Y. Huang, J. Tang and J. Liu, *Carbon*, 2020, **167**, 270–277.
3 J. Ding, H. Zhao, Q. Wang, H. Dou, H. Chen and H. Yu, *Nanoscale*, 2021, **13**, 2044.
4 B. Shen, W. Zhai and W. Zheng, *Adv. Funct. Mater.*, 2014, **24**, 4542–4548.
5 L. Peng, Z. Xu, Z. Liu, Y. Guo, P. Li and C. Gao, *Adv. Mater.*, 2017, **29**, 1700589.
6 H.-L. Li, S.-N. Xiao, H.-L. Yu, Y.-H. Xue and J.-H. Yang, *New Carbon Mater.*, 2021, **36**, 897–908.
7 L. Lv, W. Dai, J. H. Yu, N. Jiang and C. T. Lin, *New Carbon Mater.*, 2021, **36**, 930–938.
8 Z. He, Y. Yan and Z. Zhang, *Energy*, 2021, **216**, 119223.
9 Q.-Q. Kong, Z. Liu, J.-G. Gao, C.-M. Chen, Q. Zhang, G. Zhou, Z.-C. Tao, X.-H. Zhang, M.-Z. Wang, F. Li and R. Cai, *Adv. Funct. Mater.*, 2014, **24**, 4222–4228.
10 H. Lu, J. Zhang, J. Luo, W. Gong, C. Li, Q. Li, K. Zhang, M. Hu and Y. Yao, *Composites, Part A*, 2017, **102**, 1–8.
11 X. Meng, H. Pan, C. Zhu, Z. Chen, T. Lu, D. Xu, Y. Li and S. Zhu, *ACS Appl. Mater. Interfaces*, 2018, **10**, 22611–22622.
12 P. Kim, L. Shi, A. Majumdar and P. L. McEuen, *Phys. Rev. Lett.*, 2001, **87**, 215502.
13 Q. Li, C. Liu, X. Wang and S. Fan, *Nanotechnology*, 2009, **20**, 145702.
14 J. Hone, M. Whitney, C. Piskoti and A. Zettl, *Phys. Rev. B: Condens. Matter Mater. Phys.*, 1999, **59**, R2514–R2516.
15 C.-T. Hsieh, C.-E. Lee, Y.-F. Chen, J.-K. Chang and H.-S. Teng, *Nanoscale*, 2015, **7**, 18663–18670.
16 E. Zhou, J. Xi, Y. Guo, Y. Liu, Z. Xu, L. Peng, W. Gao, J. Ying, Z. Chen and C. Gao, *Carbon*, 2018, **133**, 316–322.
17 R. Zou, F. Liu, N. Hu, H. Ning, Y. Gong, S. Wang, K. Huang, X. Jiang, C. Xu, S. Fu, Y. Li and C. Yan, *ACS Appl. Mater. Interfaces*, 2020, **12**, 57391–57400.
18 Q. Chen, X. Yan, L. Wu, Y. Xiao, S. Wang, G. Cheng, R. Zheng and Q. Hao, *ACS Appl. Mater. Interfaces*, 2021, **13**, 5435–5444.
19 T.-W. Pan, W.-S. Kuo and N.-H. Tai, *Compos. Sci. Technol.*, 2017, **151**, 44–51.
20 C. Chen, Q.-H. Yang, Y. Yang, W. Lv, Y. Wen, P.-X. Hou, M. Wang and H.-M. Cheng, *Adv. Mater.*, 2009, **21**, 3541.
21 C.-M. Chen, J.-Q. Huang, Q. Zhang, W.-Z. Gong, Q.-H. Yang, M.-Z. Wang and Y.-G. Yang, *Carbon*, 2012, **50**, 659–667.
22 H. Jia, Q.-Q. Kong, X. Yang, L.-J. Xie, G.-H. Sun, L.-L. Liang, J.-P. Chen, D. Liu, Q.-G. Guo and C.-M. Chen, *Carbon*, 2021, **171**, 329–340.
23 J. Tersoff, *Phys. Rev. B: Condens. Matter Mater. Phys.*, 1988, **37**, 6991–7000.
24 N. Iwashita, C. R. Park, H. Fujimoto, M. Shiraishi and M. Inagaki, *Carbon*, 2004, **42**, 701–714.
25 G. E. Bacon, *Acta Crystallogr.*, 1951, **4**, 558–561.
26 L. H. Zou, B. Y. Huang, Y. Huang, Q. H. Huang and C. A. Wang, *Mater. Chem. Phys.*, 2003, **82**, 654–662.
27 R. E. Franklin, *Acta Crystallogr.*, 1951, **4**, 253.
28 N. Wang, M. K. Samani, H. Li, L. Dong, Z. Zhang, P. Su, S. Chen, J. Chen, S. Huang, G. Yuan, X. Xu, B. Li, K. Leifer, L. Ye and J. Liu, *Small*, 2018, **14**, 1801346.
29 M. M. Lucchese, F. Stavale, E. H. M. Ferreira, C. Vilani, M. V. O. Moutinho, R. B. Capaz, C. A. Achete and A. Jorio, *Carbon*, 2010, **48**, 1592–1597.
30 E. H. Martins Ferreira, M. V. O. Moutinho, F. Stavale, M. M. Lucchese, R. B. Capaz, C. A. Achete and A. Jorio, *Phys. Rev. B: Condens. Matter Mater. Phys.*, 2010, **82**, 125429.
31 L. G. Cancado, A. Jorio, E. H. Martins Ferreira, F. Stavale, C. A. Achete, R. B. Capaz, M. V. O. Moutinho, A. Lombardo, T. S. Kulmala and A. C. Ferrari, *Nano Lett.*, 2011, **11**, 3190–3196.
32 J.-H. Zhong, J. Zhang, X. Jin, J.-Y. Liu, Q. Li, M.-H. Li, W. Cai, D.-Y. Wu, D. Zhan and B. Ren, *J. Am. Chem. Soc.*, 2014, **136**, 16609–16617.
33 J.-W. Jiang, B.-S. Wang and J.-S. Wang, *Appl. Phys. Lett.*, 2011, **99**, 043109.
34 R. Rozada, J. I. Paredes, S. Villar-Rodil, A. Martínez-Alonso and J. M. D. Tascón, *Nano Res.*, 2013, **6**, 216–233.

35 R. Saito, A. Jorio, A. G. Souza, G. Dresselhaus, M. S. Dresselhaus and M. A. Pimenta, *Phys. Rev. Lett.*, 2002, **88**, 027401.
36 S. Jin, B. Chung, H. J. Park, B. V. Cunning, J.-H. Lee, A. Yoon, M. Huang, H. Seo, D. Lee, Z. Lee, R. S. Ruoff and S. Ryu, *Adv. Funct. Mater.*, 2020, **30**, 2005381.
37 W. Xie, L.-T. Weng, K. M. Ng, C. K. Chan and C.-M. Chan, *Carbon*, 2017, **112**, 192–200.
38 Z. Wang, Q. Yao, C. Neumann, F. Boerrnert, J. Renner, U. Kaiser, A. Turchanin, H. J. W. Zandvliet and S. Eigler, *Angew. Chem., Int. Ed.*, 2020, **59**, 13657–13662.
39 B.-c Wang, Q. Cao, W. Shao and Z. Cui, *Phys. Chem. Chem. Phys.*, 2022, **24**, 5546–5554.
40 J. Chen, J. H. Walther and P. Koumoutsakos, *Adv. Funct. Mater.*, 2015, **25**, 7539–7545.
41 Y. Zhu, L. Li, C. Zhang, G. Casillas, Z. Sun, Z. Yan, G. Ruan, Z. Peng, A.-R. O. Raji, C. Kittrell, R. H. Hauge and J. M. Tour, *Nat. Commun.*, 2012, **3**, 1225.
42 Y. Yang, N. D. Kim, V. Varshney, S. Sihn, Y. Li, A. K. Roy, J. M. Tour and J. Lou, *Nanoscale*, 2017, **9**, 2916–2924.
43 F. D. Novaes, R. Rurali and P. Ordejon, *ACS Nano*, 2010, **4**, 7596–7602.
44 X. Guo, S. Cheng, W. Cai, Y. Zhang and X.-A. Zhang, *Mater. Design*, 2021, **209**, 109936.